

**MOLECULAR GAS PROPERTIES OF THE STARBURST
NUCLEUS OF IC 342:
High Resolution $^{13}\text{CO}(2-1)$ Imaging**

David S. Meier, Jean L. Turner

Department of Physics and Astronomy, University of California, Los Angeles, CA
90095-1562

email: meierd,turner@astro.ucla.edu

and

Robert L. Hurt

Infrared Processing and Analysis Center, MS 100-22, California Institute of Technology,
Pasadena, CA 91125

email: hurt@ipac.caltech.edu

Received _____; accepted _____

to appear in the Astrophysical Journal

ABSTRACT

We present a map of the $J = 2 - 1$ transition of ^{13}CO in the starburst nucleus of IC 342 made with the Owens Valley Millimeter Array. The interferometric ^{13}CO map allows us to directly compare with $^{12}\text{CO}(1-0)$, $^{12}\text{CO}(2-1)$, and $^{13}\text{CO}(1-0)$ maps of nearly identical ($\sim 4.5''$) resolution. While all four transitions show a similar basic morphology, there are spatial differences between the ^{12}CO and ^{13}CO transitions which show up in ratio maps. In particular, the $^{13}\text{CO}(2-1)/^{13}\text{CO}(1-0)$ ratio has a markedly different distribution across the nuclear region than does $^{12}\text{CO}(2-1)/^{12}\text{CO}(1-0)$, indicating that ^{12}CO and ^{13}CO trace different components of the molecular gas. These differences are explained if ^{12}CO traces the warm, PDR “skins” of the clouds and ^{13}CO traces the cooler, interior portions constituting the bulk of the molecular gas. We derive excitation temperatures for the bulk of the cloud mass to be $\sim 10 - 20$ K and densities of $\sim 10^{3.7} \text{ cm}^{-2}$ along the molecular mini-spiral.

Subject headings: galaxies:individual(IC342)—galaxies:ISM—galaxies:nuclei—galaxies:starburst—radio lines:galaxies

1. Introduction

The $^{12}\text{CO}(1-0)$ line is a universal and sensitive tracer of molecular gas in galaxies (Young & Scoville 1991). Because it is easily excited and thermalized, $^{12}\text{CO}(1-0)$ is observed to be optically thick almost everywhere it is seen. The high opacity of the CO line constrains the information that can be derived from it, although it does appear to be a good temperature and mass tracer under certain well-defined conditions (Solomon et al. 1987). But it is important to study the behavior of this molecule in unusual conditions, such as starburst regions, since it is so ubiquitous and easily detected.

IC 342 is an excellent subject to study since it is one of the closest spiral galaxies (D ~ 1.8 Mpc; Ables 1971; McCall 1989; Madore, & Freedman 1992; Karachentsev & Tikhonov 1993) with substantial nuclear star formation (Becklin et al. 1980; Turner & Ho 1983)(Table 1). The molecular clouds in the center of IC 342 have been studied extensively (Morris & Lo 1978; Young & Scoville 1982; Young & Sanders 1986; Eckart et al. 1990; Sage & Solomon 1991; Rieu et al. 1992; Xie, Young, & Schloerb 1994; Paglione et al. 1995; Jackson et al. 1995). Estimated temperatures of the molecular clouds vary widely, ranging from values of $T_{\text{ex}} \sim 10$ K to more than 100 K (Rieu et al. 1992; Martin & Ho 1979;1986; Ho, Turner & Martin 1987; Wall & Jaffe 1990; Steppe et al. 1990, Harris et al. 1991; Irwin & Avery 1992; Güsten et al. 1993) Recently, IC 342 has been studied at a high resolution, using aperture synthesis, in $^{12}\text{CO}(1-0)$ (Lo et al. 1984; Ishuzuki et al. 1990; Levine et al. 1993), $^{13}\text{CO}(1-0)$ (Turner & Hurt 1992 [TH92]; Wright et al. 1993), $^{12}\text{CO}(2-1)$ Turner, Hurt, & Hudson 1993 [THH93], NH_3 (Ho et al. 1990), and HCN (Downes et al. 1992). Both single-dish and interferometric observations have shown ^{12}CO line ratios that indicate the ^{12}CO emission is optically thin despite the large column densities implied by the ^{12}CO intensities (Ho, Turner & Martin 1987; Eckart et al. 1990; THH93).

To reconcile this apparently contradictory results, we have made aperture synthesis

maps of $^{13}\text{CO}(2-1)$. Due to lower optical depth, the ^{13}CO transitions potentially provide deeper and more representative probes of the gas than the low J ^{12}CO lines. We are now able to obtain interferometric maps of $^{13}\text{CO}(2-1)$ and $^{13}\text{CO}(1-0)$ at nearly identical resolutions ($\sim 4.5''$) to accurately determine line ratios. By comparing ratio maps of the thinner ^{13}CO transitions with their thicker ^{12}CO counterparts, we investigate how molecular gas temperatures, densities, and general gas properties vary across the starburst region.

2. Observations

The observations of the $^{13}(2-1)$ transition (220.40 GHz) were made between 1990 December 26, and 1991 January 31 with the 3-element Owens Valley Millimeter Array (OVRO) (Woody et al. 1989; Padin et al. 1991). System temperatures were 800 - 900 K (SSB). A spectrometer with 32, 5 MHz, channels was used for the transition. Phase calibration was done using the quasar 0224+671. The absolute positional uncertainty is estimated to be $\leq 1''$ at 1.3 mm. Absolute flux calibration was done using Uranus as the primary calibrator and the quasar 3C 454.3 as a secondary calibrator. Uncertainties in the absolute 1 mm flux of Uranus and 3C 454.3 give an estimated accuracy of 20% - 25% in absolute flux scale. We compare these $^{13}\text{CO}(2-1)$ observations with the previous OVRO observations of $^{13}\text{CO}(1-0)$, $^{12}\text{CO}(1-0)$ and $^{12}\text{CO}(2-1)$. The details of these observations are summarized in Table 2 (see Levine et al. 1993 [$^{12}\text{CO}(1-0)$], TH92 [$^{13}\text{CO}(1-0)$] and THH93 [$^{12}\text{CO}(2-1)$]) for full details).

To estimate how much extended flux the interferometer resolved out of the $^{13}\text{CO}(2-1)$ map, it was compared with the fully-sampled, single-dish maps from the 30m IRAM telescope (Eckart et al. 1990) at $14''$ resolution, and the FCRAO 14m telescope (Xie et al. 1994) at $23''$ resolution. The peak integrated intensities in the OVRO map when convolved to the $14''$ and $23''$ beamsizes are 25 K km s^{-1} and 15 K km s^{-1} , respectively. This

corresponds to $\sim 80\%$, and 100% of the peak intensity of the respective single-dish maps. So it appears that little, if any, of the $^{13}\text{CO}(2-1)$ flux has been missed by the interferometer. This also is the case for $^{12}\text{CO}(2-1)$, (THH93) and $^{13}\text{CO}(1-0)$ (TH92), but not the case for $^{12}\text{CO}(1-0)$, for which $\sim 20\%$ is resolved out.

All of the maps were made and CLEANed using the NRAO AIPS package. The maps were naturally weighted and primary beam corrected. The OVRO primary beam is $\sim 64''$ at (1-0) and $\sim 34''$ at (2-1) (FWHM). In making the integrated intensity maps only emission greater than 1.3σ was included. Structures extended on scales larger than $\sim 20''$ is resolved out of the maps by the 10 k λ minimum baselines.

3. RESULTS

3.1. Spatial Distribution of ^{13}CO gas in IC 342

The integrated intensity maps of the four CO transitions are plotted to the same scale in Figure 1a-d. In Figure 2, we display a schematic representation of the important regions. The basic morphology of the $^{12}\text{CO}(1-0)$ is an open two-armed spiral pattern extending more than $60''$ in the north-south direction, which we refer to as the “arm” region (Lo et al. 1984; Ishizuki et al. 1990; Levine et al. 1993). The emission from the inner portion of the arm region is dominated by three major peaks lying about 40 pc to the northeast (C), southeast (A), and southwest (B+E) of the dynamical center (we use the letter designations of Downes et al. 1992). This three peak structure is seen in all the low CO transitions as well as in HCN (Downes et al. 1992). The starburst fills the “central trough” in CO, with the strongest region of star-formation coming from the southwestern edge, towards the interface with GMC B (Turner & Ho 1983; Figure 5). This region with the strongest star formation as traced by radio continuum emission is called the “starburst region.” A region

of $^{12}\text{CO}(2-1)/^{12}\text{CO}(1-0)$ peaks are found near GMC C (§3.3). This region is referred to as the “Eastern Ridge” (Eckart et al. 1990). Although the CO transitions all display a similar basic structure there are significant differences. In this paper we focus on these differences and their implications for the gas in the inner nuclear region.

The $^{13}\text{CO}(2-1)$ channel maps are presented in Figure 3. When corrected for the Rayleigh-Jeans approximation, $T_r = (h\nu/k)/\ln(h\nu/kT_b + 1)$, the radiation temperatures found for the $^{13}\text{CO}(2-1)$ channels range from a 3σ value of $T_r = 3.4$ K to a peak of 7.7 K. The radiation temperatures for the other transitions are: 6 K - 24 K for $^{12}\text{CO}(1-0)$, 5 K - 30 K for $^{12}\text{CO}(2-1)$, and 2 K - 5 K for $^{13}\text{CO}(1-0)$. Emission is present in channels $V_{LSR} = -5 \text{ km s}^{-1}$ to 75 km s^{-1} with higher velocities in the northeast. Measured antenna temperatures and integrated intensities of each transition are listed in Table 3 for various locations across the nucleus.

The three peaks seen in the $^{13}\text{CO}(2-1)$ map generally coincide with the position of the peaks found in the other CO transitions. However, unlike $^{12}\text{CO}(2-1)$ which peaks in the northeast, the ^{13}CO emission peaks towards the southwest. Of all the transitions observed, $^{13}\text{CO}(2-1)$ most closely reflects the structure detected in HCN by Downes et al. (1992). The southwest $^{13}\text{CO}(2-1)$ intensity peak is a blend of their peaks, B and E, (as seen in the $11.2 - 31.6 \text{ km s}^{-1}$ channels). The field of view of the CO(2-1) maps are smaller than those of the CO(1-0) maps due to smaller primary beam at 1.3 mm. Even so, the detection of $^{13}\text{CO}(2-1)$ is not limited by the primary beam as is the case for $^{12}\text{CO}(2-1)$. In the Arm regions, the sensitivities are high enough to detect $^{13}\text{CO}(2-1)$ if it has the same relative distribution as ^{12}CO . The fact that we don’t implies $^{13}\text{CO}(2-1)$ must be concentrated more strongly to the GMCs than the other CO transitions.

3.2. Molecular Gas Column Densities

Molecular gas column densities can be obtained from ^{12}CO using a standard conversion factor or from the $^{13}\text{CO}(1-0)$ line assuming the transition is optically thin:

$$N(\text{H}_2)_{^{13}\text{CO}} = 2.41 \times 10^{14} \frac{[\text{H}_2]}{[^{13}\text{CO}]} \frac{e^{\frac{5.29}{T_{\text{ex}}}}}{(e^{\frac{5.29}{T_{\text{ex}}}} - 1)} I_{^{13}\text{CO}} \text{ (K km s}^{-1}\text{)}.$$

Adopting isotopic abundance ratios for IC 342 of $[^{12}\text{CO}]/[^{13}\text{CO}] = 40$ and $[^{12}\text{CO}]/[\text{H}_2] = 8.5 \times 10^{-5}$ for IC 342 (Henkel & Mauersberger 1993; Frerking et al. 1982), the observed ^{13}CO integrated intensities yield column densities ranging from $N(\text{H}_2) \simeq 4 \times 10^{21}$ to $3 \times 10^{22} \text{ cm}^{-2}$. (We have adopted a value of $T_{\text{ex}} = 20 \text{ K}$, which is lower than the dust temperature of Rickard & Harvey 1984, but consistent with the excitation temperature implied by the ^{13}CO line ratios (§4.1.2))

Using the Galactic conversion factor of $X_{\text{CO}} = 2.3 \times 10^{20} \text{ cm}^{-2} (\text{K km s}^{-1})^{-1}$ (Strong et al. 1988), derived column densities range from $1.5 \times 10^{22} \text{ cm}^{-2}$ - $2 \times 10^{23} \text{ cm}^{-2}$ over beamsizes of $\sim 40 \text{ pc}$ (Figure 1a). Assuming the central peaks are single spherical GMCs, we derive beam averaged densities of $\langle n_{\text{H}_2} \rangle \simeq 1.3 \times 10^3 \text{ cm}^{-3}$ and individual cloud masses of $\langle M_{\text{cloud}} \rangle \simeq 1.4 \times 10^6$. Densities are likely much higher than the average $\langle n_{\text{H}_2} \rangle$ over portions of the cloud, consistent with the presence of HCN emission (Downes et al. 1992). The H_2 masses we derive assuming ^{13}CO is optically thin are a factor of four lower than those derived from $^{12}\text{CO}(1-0)$. However, it is likely that ^{13}CO column densities are underestimates of the true $N(\text{H}_2)$ due to optical depth effects (§4.3).

3.3. CO Line Ratio Maps

In Figure 4a-d, the line ratio maps are presented. We follow the nomenclature of Aalto (1994) and designate $r_{12} = ^{12}\text{CO}(2-1)/^{12}\text{CO}(1-0)$, $r_{13} = ^{13}\text{CO}(2-1)/^{13}\text{CO}(1-0)$, $R_{10} = ^{12}\text{CO}(1-0)/^{13}\text{CO}(1-0)$, and $R_{21} = ^{12}\text{CO}(2-1)/^{13}\text{CO}(2-1)$. In generating the ratio maps,

the integrated intensity maps were convolved to matching the beamsizes, divided, and then blanked anywhere emission was $< 4\sigma$ in either map. Errors in the ratio maps are conservatively estimated to be $\leq 35\%$ in magnitude and $\leq 2''$ in position.

The r_{13} ratio map has relatively constant values of 0.8 - 0.9 over much of the central mapped region (Figure 4b). At distances greater than about 150 pc towards the northeast, the r_{13} ratio decreases to values of ~ 0.3 . The r_{13} ratio has only one peak with a value of ~ 1.7 . The location of the r_{13} peak is *not* coincident with the peak in the r_{12} ratio map associated with starburst region, but northeast of that peak, at the central trough. The r_{12} ratio map, by contrast, shows a fair amount of structure (THH93; Figure 4a). The r_{12} ratio ranges from 0.9 to 3.7, with an average across the region of approximately 1.4. Along the Eastern Ridge peak values of $r_{12} \sim 2.2$ are found. The r_{12} peak at the overlap of the nuclear starburst region and the southern CO intensity peak has a value of 2.1. The ratio maps are consistent with the single-dish ratio maps of Eckart et al. (1990), given the differences in beamsizes.

The isotopic ratio maps, R_{10} and R_{21} are presented in Figure 4c & 4d. Values of 15 - 30 are found in the regions behind the spiral arms, both north and south of the nucleus. The ratio in the central trough is $R_{10}=11.3$. The lowest values of $R_{10} \sim 3 - 6$ and $R_{21} \sim 5 - 9$ are seen towards the GMCs A, C & E. In agreement with Wright et al. (1993), we find the R_{10} ratio varies systematically across the nucleus. R_{10} is uniformly lower on the leading, compressed side of the density wave and becomes higher than is commonly observed in the Galaxy, on the trailing side of the spiral arm. Large R_{21} ratios are also seen in the “arm” and “off-arm” regions. The precise value of R_{21} is somewhat less certain, due to the weakness of $^{13}\text{CO}(2-1)$ but must be very high (> 25).

4. DISCUSSION

4.1. CO(2-1)/CO(1-0) Ratios (r_{12} & r_{13}): Cloud Temperatures

In theory, r_{12} and r_{13} , can be used to estimate temperatures of molecular clouds. In practice, this is difficult unless one simultaneously studies other molecular transitions including isotopes of different opacities (Sakamoto 1993; Aalto 1995). Assuming LTE:

$$r_i = \frac{({}^iT_r(2-1) - {}^iT_{BG}(2-1))(1 - e^{-i\tau_{21}})}{({}^iT_r(1-0) - {}^iT_{BG}(1-0))(1 - e^{-i\tau_{10}})}$$

where i denotes the isotopic species, iT_r is the Rayleigh-Jeans corrected brightness temperature of the respective transitions and τ is the optical depth of each respective transition. ${}^iT_{BG}(1-0)$ and ${}^iT_{BG}(2-1)$ are the Rayleigh-Jeans corrected brightness temperatures of the cosmic microwave background (CMB). We can ignore the T_{BG} terms here because the uniform CMB is resolved out and will not affect ratios obtained from optically thick or strongly beam-diluted gas. A simplifying assumption often made is that both of the transitions have the same excitation temperature, T_{ex} . Under this assumption, ratios between zero and four are expected, with ratios less than one for optically thick gas. Since the Rayleigh-Jeans approximation does not hold for cool clouds at this frequency, the ratio of the measured RJ brightness temperatures for CO(2-1)/CO(1-0) is not unity, and always less than one, for optically thick gas. This fact can be exploited to estimate the gas excitation temperature.

4.1.1. r_{12} : Tracer of CO Photospheres

At first glance it would seem that $r_{12} > 1$ (Figure 4a) imply optically thin emission. However, the column densities of the gas are much higher than would be implied by optically thin emission (Wall & Jaffe 1990; TH92; Meier & Turner 1999). THH93 suggest the possibility that temperature gradients can explain the higher ratios. They propose that

heating due to the star-formation complex is occurring in photo-dissociation regions (PDRs) at the surfaces of the large molecular clouds. Since the $^{12}\text{CO}(2-1)$ transition saturates more quickly than $^{12}\text{CO}(1-0)$, it would arise preferentially in these warm, outer layers of the externally heated clouds (Crawford et al. 1985; Stacey et al. 1991; Wolfire, Hollenbach, & Tielens 1993; Hollenbach & Tielens 1997). The $^{12}\text{CO}(2-1)$ would then have a higher T_{ex} and larger brightness temperatures than $^{12}\text{CO}(1-0)$. The recent detection of $2.12\mu\text{m}$ $\text{H}_2(1-0)$ emission from this region also supports the existence of hot (≤ 2000 K), “PDR” gas (Böker et al. 1997).

For the Eastern Ridge, a similar explanation seem likely for the high r_{12} . In Figure 5, the HST¹ $\text{H}\alpha$ image of IC 342 is overlaid on the $^{13}\text{CO}(2-1)$ and 2 cm contours (2 cm: Turner & Ho 1983; $\text{H}\alpha$: Gallagher et al 1999). HII regions extend along the outside edge of both CO arms as well as towards the starburst core associated with the 2 cm peak. The 2 cm radio continuum maps (Figure 4) show a secondary peak at the Eastern Ridge. This is the location of warm NH_3 gas (≥ 70 K Martin & Ho 1986; Ho et al. 1990) and high excitation $^{12}\text{CO}(6-5)$ (Harris et al. 1991). An increase in the $\text{HeI}/\text{B}\gamma$ ratio is seen at this location, indicating the presence of substantial numbers of hot ($T_* \geq 36,000$ K), massive stars, which may provide the ionization and heating for the Eastern Ridge (Böker et al. 1997).

Towards the southwest edge of the map $r_{12} \sim 4$. The emission from this off-arm region appears to be warm and optically thin in the usual sense, since the CO emission is weak here and there is bright $\text{H}\alpha$ emission. Because these are ratios of weak emission and near the edge of the primary beam, we do not discuss them in detail. But it does appear that

¹Based on observations made with the NASA/ESA Hubble Space Telescope, obtained from the data archive at the Space Telescope Science Institute. STScI is operated by the Association of Universities for Research in Astronomy, Inc. under the NASA contract NAS 5-26555.

temperatures of ≥ 50 K may be present at some of these off-arm locations.

We conclude, in agreement with Aalto (1994), that the r_{12} ratio may not reflect the the excitation conditions of the bulk of the molecular gas. In fact, the ^{12}CO line ratios appear “optically thin” because $^{12}\text{CO}(2-1)$ intensity is dominated by the outer photospheres of the clouds which are hot, have steep temperature gradients, and are a limited fraction of the total column density.

4.1.2. r_{13} : A Better Tracer of Bulk Gas Properties?

Because ^{13}CO is less abundant than ^{12}CO and samples greater cloud depths, its lines should be dominated less by outer PDR regions which effect the ^{12}CO . If temperature decreases with depth into the cloud, then the T_{ex} derived from ^{13}CO will be lower than those derived from ^{12}CO . Since ^{13}CO traces more of the gas, local temperature gradients should also be averaged out giving smoother, more constant T_{ex} -like ratios than does ^{12}CO . If the high r_{12} are indeed due to skin depth effects in the outer layers of the clouds, then one would expect much less of an effect on r_{13} . On the other hand, if ^{12}CO is truly optically thin throughout the molecular cloud, then so must ^{13}CO and both the r_{12} and r_{13} ratios will reflect the same excitation structure.

It is clear from Figures 4a & b that the r_{13} map of IC342’s nucleus does not resemble the r_{12} map. The r_{13} ratios are quite low (0.3 - 1.7) and relatively uniform. In addition, the spatial structure of the peaks and lows are completely different for r_{12} and r_{13} . From our r_{12} and r_{13} maps we see that ^{12}CO and ^{13}CO transitions in the nucleus clearly *are not* tracing the same gas and are inconsistent with uniform temperature excitation models.

We discuss three possible explanations for why the r_{13} ratios are low (≤ 1). First, the ^{13}CO emission could be optically *thin*, cold, and trace only the cores of the molecular

clouds. Although assuming ^{13}CO is optically thin yields excitation temperatures of $7 \sim 13$ K, similar to temperatures of GMCs in the disk of the Galaxy (Scoville & Good 1988), densities and temperatures in the center of IC 342 appear to be higher than those of Galactic disk clouds (Martin & Ho 1986; Downes et al. 1992; Wall & Jaffe 1990; §4.1.3). Moreover, the ^{13}CO antenna temperatures (~ 7.5 K) are already quite high. For this option to be true, ^{13}CO filling factors must be unity, implying the cold interior cores must be ≥ 40 pc in size. HCN measurements suggest lower filling factors, and tidal considerations also favor smaller, denser clouds (Downes et al 1992). We feel this interpretation is unlikely.

A second possible explanation for r_{13} ratios of < 1 is that the ^{13}CO lines are becoming optically thick ($\tau > 1$), a possibility mentioned by Eckart et al. (1990) and Wall & Jaffe (1990). At the location of the intensity peaks, $r_{13} < 1$, consistent with the large optical depths. r_{13} ratios of $0.8 \sim 0.9$ imply $T_{ex} = 14 \sim 27$ K (LTE). The antenna temperatures in this region imply that the ^{13}CO emitting clouds have an areal filling factor of $f_b \sim 0.25 - 0.5$, similar to what is found for HCN (Downes et al. 1992). This filling factor gives cloud densities of $\sim 1 \times 10^4 \text{ cm}^{-3}$, (using the ^{12}CO column densities), again more in line with what is seen in HCN emission (Downes et al. 1992). This is the interpretation we favor.

A third possible explanation for the low r_{13} ratios is that ^{13}CO emission is subthermally excited across the three GMCs. This is unlikely given the fact that we estimate a density of $< n_{H_2} > \sim 10^{3-4}$ which is at or above the critical density of CO in either transition. The fact that HCN (Downes et al. 1992) and CS (Xie, Young & Schloerb 1994; Paglione et al. 1995) is detected indicates that the densities are high in these clouds. For the “arm” regions, where the r_{13} ratio drops to ~ 0.3 , subthermal emission probably is a good explanation of the ^{13}CO gas excitation.

One region where ^{13}CO appears to be genuinely optically thin is the central trough. The peak of the r_{13} ratio map in this region is greater than unity. It lies at the site of an

obvious decrease in emission in all four CO integrated intensity maps. The high r_{13} values seen here requires that the molecular gas to have both high temperatures and low optical depths.

4.1.3. LVG Modeling of ^{13}CO

To further investigate the validity of our results, we have run a sample of large velocity gradient (LVG) radiative transfer models for comparison with our LTE models (Goldreich & Kwan 1974; De Jong, Chu & Dalgarno 1975). As we have already shown from the comparison of r_{12} and r_{13} , ^{12}CO and ^{13}CO do not trace the same gas. ^{12}CO emission is influenced by strong gradients at the cloud surfaces, which LTE and LVG models cannot handle. Since ^{13}CO lines are less affected by these problems we model only the ^{13}CO . Constraints on the velocity gradient (dv/dr) in IC 342’s nucleus are estimated directly from the data. The FWHM linewidths determined at each position, combined with the resolved sizes of the clouds (or a size based on a filling factor of $f_a \sim 0.33$ (§4.1.2) for the non-cloud sites) are used to estimate the local dv/dr at each position. Typical values range from 3 - 5 $\text{km s}^{-1} \text{pc}^{-1}$. The velocity gradient is uncertain to at least a factor of two, but the results are relatively insensitive to dv/dr over this range. All models assume a ^{13}CO an abundance of 2×10^{-6} (§3.2).

LVG modeling of the GMCs constrain the temperature, but not the density, which is typical for CO above its thermalization density (Figure 6). At the locations of the GMCs, the LVG models obtain $T_K \simeq 10 - 20 \text{ K}$, $^{13}\tau_{10} \sim 1.5 - 8.0$, and $\langle n_{H_2} \rangle > 10^{3.7}$, similar to the values obtained from LTE modeling. In the region of the central trough, where LTE modeling is unable to yield a clear answer, LVG modeling shows that the density is better constrained than the temperature. We obtained $T_K \simeq 45 \text{ K}$, $^{13}\tau_{10} \sim 0.04 - 0.2$, and $\langle n_{H_2} \rangle \simeq 10^{3.1}$ for this region.

4.2. The Isotopic Ratios, R_{10} and R_{21} , and CO optical depth

We map R_{21} and compare it to R_{10} in the IC 342 starburst region (Figure 4c & 4d). The particularly low values ($\sim 3 - 4$) of R_{10} and R_{21} at GMCs A, C & E reflect high optical depths in these clouds. Since ^{13}CO appears optically thick in these regions, an isotopic ratio of unity is expected unless ^{12}CO and ^{13}CO have *different* filling factors or higher ^{12}CO has higher excitation temperatures than ^{13}CO . The ^{12}CO excitation temperatures appears higher than the ^{13}CO excitation temperatures, but not enough to explain the difference. Correcting $R_{10} \sim 4$ for the higher ^{12}CO excitation temperatures implies relative filling factors of $F_a \sim 0.33$.

The gas in the “off-arm” regions appear more diffuse. The high isotopic ratios towards the off-arm regions probably reflect the fact that ^{13}CO is becoming subthermal in these lower density regions. This conclusion is consistent with the fact that the R_{21} isotopic ratios are larger than the R_{10} isotopic ratios, and that quite low (~ 0.3) r_{13} ratios are observed in these regions.

Wright et al. (1993) and TH92 suggest that the R_{10} peak at the central trough might be due to temperature effects associated with the strong star-formation complex. We have seen (§4.1.2) that the reason for this peak is that $^{13}\text{CO}(1-0)$ is optically thin here. While the temperature gradients probably play some role, the simultaneous increase in the r_{13} ratio at this location and the fact that the R_{10} peak is off of the starburst region, indicates that optically thin ^{13}CO is the dominate cause for the higher ratio.

4.3. Is ^{12}CO a Good Tracer of H_2 in IC 342?

In using millimeter emission line observations as tracers of molecular hydrogen, we are generally limited to either optically thin but temperature sensitive lines (CO “rare”

isotopes), lines which trace high density gas but may miss the lower density gas (HCN, CS), or optically thick lines (^{12}CO). The question raised is: To what extent do each of these successfully trace molecular gas in the starburst nuclei?

The column densities predicted from ^{12}CO using the standard conversion factor and from the optically thin ^{13}CO lines differ in IC 342, but moderate ^{13}CO optical depths seem to be the reason, not large differences from the Galactic CO conversion factor (§4.1.2; Meier & Turner 1999). In fact, LVG modeling suggests that $^{12}\text{CO}(1-0)$ emission is a better mass tracer than ^{13}CO estimates under the optically thin assumption. LVG models yield peak column densities of $1.9 \times 10^{23} \text{ cm}^{-2}$, close to what is obtained from the $^{12}\text{CO}(1-0)$ conversion factor.

In IC 342 it is found that nearly all the molecular tracers have the same basic morphology. However important differences between the tracers exist as indicated by differences in the line ratios, r_{12} , r_{13} , R_{10} , and R_{21} . In IC 342, the ratios seems to indicate that ^{12}CO does not trace the same portion of molecular clouds as ^{13}CO (particularly striking in the difference between r_{12} and r_{13} ratios). ^{12}CO is still reliable in tracing the morphology and amount of the molecular gas since it traces the outer layers of the cloud complexes. While the outer highly emissive skins of the molecular clouds traced by the ^{12}CO seem to do a good job of representing cloud morphology, they poorly represent the physical properties of the molecular clouds, such as the excitation temperatures, kinetic temperatures and densities of the bulk of the molecular gas. For the bulk excitation properties of the gas, it appears that ^{13}CO is the more reliable probe.

5. Summary

The aperture synthesis map of $^{13}\text{CO}(2-1)$ in the nucleus of IC 342 shows that the ^{13}CO emission is moderately optically thick, and strongly confined to the cloud peaks found in previous CO and HCN interferometer maps. ^{13}CO emission appears to be dominated by the interiors of the clouds where the temperatures are lower and relatively uniform. ^{13}CO ratios imply excitation temperatures of $\sim 10 - 20$ K. These gas temperatures are cooler than indicated by ^{12}CO (>30 K), NH_3 (70 K), FIR (43 K) dust emission, and H_2 (≤ 2000 K). LVG models and ^{13}CO filling factors indicate that the individual clouds have densities of $\langle n_{\text{H}_2} \rangle \simeq 10^{3.7-4.5} \text{ cm}^{-3}$, consistent with HCN observations.

Substantial differences in the r_{12} and r_{13} ratio maps are observed. The differences between r_{12} and r_{13} clearly demonstrate that ^{13}CO does *not* trace the same molecular gas component as the ^{12}CO transitions. Although the ^{12}CO and ^{13}CO do not originate from the same gas, the ^{12}CO does seem to map the molecular structure in IC 342 with good fidelity. ^{13}CO is more reliable for investigating the intrinsic gas physical conditions, such as temperature and density.

The favored picture of the molecular gas properties towards the center of IC 342 is the following: Molecular gas appears to be characterized by dense molecular clouds with the bulk of the molecular gas at temperatures around 10-20 K. The clouds are surrounded by an outer PDR “skin” and intercloud medium that consists of much hotter (>50 K) layers. Layers of different temperatures are seen by different transitions, with the optically thickest transitions (particularly the higher J ^{12}CO transitions) tracing the highest temperatures.

We thank Steve Padin, Steve Scott, and Dave Woody for assistance with the observations. We also thank the anonymous referee for useful comment that helped improve the presentation of the paper. This work was supported in part by NSF grant AST94-17968.

R.L.H. acknowledges the support of the Jet Propulsion Laboratory, California Institute of Technology, which is operated under contract with the National Aeronautics and Space Administration. The Owens Valley Millimeter Interferometer is operated with support from the California Institute of Technology and the National Science Foundation.

REFERENCES

- Aalto, E. S. 1994, PhD Dissertation, Chalmers University of Technology
- Aalto, S., Booth, R. S., Black, J. H. & Johansson, L. E. B. 1995, *A& A*, 300, 369
- Ables, A. D. 1971, *Publ. US Naval Obs.*, Ser. II, 20 79
- Arimoto, N., Sofue, Y., & Tsujimoto, T. 1995, *PASJ*, 48, 275
- Becklin, E. E., Gatley, I., Mathews, K., Neugebauer, G., Sellgren, K., Werner, M. K., & Wynn-Williams, C. G. 1980, *ApJ*, 236, 441
- Böker, T., Förster-Schreiber, N. M., & Genzel, R. 1997, preprint
- Crawford, M. K., Genzel, R., Townes, C. H., & Watson, D. M. 1985, *ApJ*, 291, 755
- Crosthwaite, L. P. et al. 1998, in prep.
- De Jong, T., Chu, S.-I., & Dalgarno, A. 1975, *ApJ*, 199, 69
- de Vaucouleurs, G., de Vaucouleurs, A., & Corwin, H. G 1976, *Second Reference Catalog of Bright Galaxies* (Austin:Unvi. Texas Press)
- Downes, D., Radford, S. J. E., Giulloteau, S., Guelin, M., Greve, A., & Morris, D. 1992, *A&A*, 262, 424
- Eckart, A., Downes, D., Genzel, R., Harris, A. I., Jaffe, D. T., & Wild, W. 1990, *ApJ*, 348, 434
- Frerking, M A., Langer, W. D., & Wilson, R. W. 1982, *ApJ*, 262, 590
- Gallagher, J. S. et al., 1998, in prep.
- Goldreich, P., & Kwan, J. 1974, *ApJ*, 189, 441

- Güsten, R., Serabyn, E., Kasemann C., Schinckel, A., Schneider, G., Schulz, A., & Young, K. 1993, *ApJ*, 402, 537
- Harris A. I., Hills, R. E., Stutzki, J., Graf, U. U., Russell, A. P. G., & Genzel, R. 1991, *ApJ*, 382, L79
- Henkel, C., & Mauersberger, R. 1993, *A&A*, 274, 730
- Ho, P. T. P., Turner, J. L., & Martin, R. N. 1987 *ApJ*, 322, L67
- Ho, P. T. P., Martin, R. N., Turner, J. L., & Jackson, J. M. 1990, *ApJ*, 355, L19
- Hollenbach, D. J., & Tielens, A. G. G. M. *ARA&A* 1997, 35, 179
- Irwin, J. A. & Avery, L. W. 1992, *ApJ*, 388, 328
- Ishizuki, S., Kawabe, R., Ishiguro, M., Okumura, S. K., Morita, K.-I., Chikada, Y., & Kasuga, T. 1990, *Nature*, 344, 224
- Jackson, J. M., Paglione, T. A. D., Carlstrom, J. E., & Nguyen-Q-Rieu 1995, *ApJ*, 438, 695
- Karachentsev, I. D., & Tikhonov, N. A. 1993, *A&AS*, 100, 227
- Levine, D., Turner, J. L., & Hurt, R. L. 1993, in *IAU Colloq. 140, Astronomy with Millimeter and Submillimeter Wave Interferometry*, ed. M. Ishiguro pg. 339
- Lo, K. Y. et al., 1984, *ApJ*, 282, L59
- Madore, B. F., & Freedman, W. L. 1992, *PASP*, 104, 362
- Maloney, P., & Black, J. H. 1988, *ApJ*, 325, 389.
- Martin, R.N., & Ho, P.T.P. 1979, *A&A*, 74, L7
- Martin, R.N., & Ho, P.T.P. 1986, *ApJ*, 308, L7

- McCall, M. L. 1989, AJ, 97, 1341
- Morris, M., & Lo, K. Y. 1978, ApJ, 223, 803
- Nguyen-Q-Rieu, Jackson, J.M., Henkel, C., Bach. T., & Mauersberger, R. 1992, ApJ, 399, 521
- Padin, S., Scott, S. L., Woody, D. P., Scoville, N. Z., Seling, T. V., Finch, R. P., Ciovanine, C. J., & Lowrance, R. P. 1991, PASP, 103, 461
- Paglione, T.A.D., Jackson, J.M., Ishizuki, S., & Nyugen-Q-Rieu 1995, AJ, 109, 1716
- Rickard, L. J., & Harvey, P. M. 1984, AJ, 89, 1520
- Sage, L. J. & Solomon, P. M. 1991, ApJ, 380, 392
- Sakamoto, S. 1993, PhD Dissertation, University of Tokyo
- Sakamoto, S. 1996, ApJ, 462, 215
- Scoville, N. Z., & Good, J. C. 1989, ApJ, 339, 149
- Solomon, P. M., Rivolo, A. R., Barrett, J. & Yahl, A. 1987, ApJ, 319, 730
- Stacy, G. J., Geis, N., Genzel, R., Lugten, J. B., Poglitsch, A., Sternberg, A., & Townes, C. H. 1991, ApJ, 373, 423
- Steppe H., Mauersberger, R., Shullz, A., & Baars, J. W. M. 1990, A&A, 233, 410
- Strong, A. W. et al., 1988, A&A, 207, 1
- Turner, J. L., & Ho, P. T. P. 1983, ApJ, 268, L79
- Turner, J. L., Hurt, R. L. 1992, ApJ, 384, 72 (TH92)
- Turner, J. L., Hurt, R. L., & Hudson, D. Y. 1993, ApJ, 413, L19 (THH93)

- Wall, W. F., & Jaffe, D. T. 1990, *ApJ*, 361, L45
- Wolfire, M. G., Hollenbach, D., & Tielens, A. G. G. M. 1993, *ApJ*, 402, 195
- Woody, D. P., Scott, S. L., Scoville, N. Z., Mundy, L. G., Sargent, A. I., Padin, S., Tinney, C. G., & Wilson, C. D., 1989, *ApJ*, 337, L41
- Wright, M. C. H., Ishizuki, S., Turner, J. L., Ho, P. T. P., & Lo, K. Y. 1993, *ApJ*, 406, 470
- Xie, S., Young, J., & Schloerb, F. P. 1994, *ApJ*, 412, 434
- Young J. S., & Scoville, N. Z. 1982, *ApJ*, 258, 467
- Young J. S., & Scoville, N. Z. 1991, *ARA&A*, 29, 581
- Young J. S., & Sanders, D. B. 1986, *ApJ*, 302, 680

Table 1. IC 342 Basic Data

Characteristic	Value	Reference ^a
Revised Hubble Class	Sab(rs)cd	1
Dynamical Center	$\alpha(2000) = 03^h46^m48^s.7 \pm 0.^s3$ $\delta(2000) = +68^\circ05'46''.8 \pm 2''$	2
$2\mu\text{m}$ peak	$\alpha(2000) = 03^h46^m48^s.3 \pm 0.^s3$ $\delta(2000) = +68^\circ05'46''.8 \pm 2''$	4
ℓ^{II}	138.2°	1
b^{II}	$+10.6^\circ$	1
V_{lsr}	35 kms^{-1}	3
Adopted Distance	1.8 Mpc	5
Inclination Angle	30°	6
Position Angle	39.4°	6
B_T	9.16 mag	1

^a(1) de Vaucouleurs, de Vaucouleurs & Corwin 1976; (2) Turner & Hurt 1992; (3) This Paper (4) Becklin et al. 1980; (5) McCall 1989; (6) Crosthwaite et al. 1998

Table 2. Observational Data

Transition ^a	Frequency (GHz)	Date	ΔV_{chan} $km\ s^{-1}$	ΔV_{band} $km\ s^{-1}$	Beamsize (arcsec; deg)	Noiselevel (K / Jy Bm ⁻¹)
¹² CO(1-0) ^b	115.271	3/15/91 - 6/9/91	2.6	82.2	2.7x2.6; 72.1	1.3 / 0.10
¹² CO(2-1) ^c	230.538	12/26/90- 1/24/91	6.5	208	4.1x3.6; -4.7	0.40 / 0.26
¹³ CO(1-0) ^d	110.201	11/90 - 6/91	5.5	87.2	4.8x3.9; 60.4	0.10 / 0.02
¹³ CO(2-1)	220.402	12/31/90 - 1/31/91	6.8	218	4.4x3.6; -0.1	0.19 / 0.12

^aPhase Center: $V_{LSR}=35\ km\ s^{-1}$

$\alpha = 03^h41^m57^s.2\ \delta = +67^\circ56'28.''0$ (B1950)

$\alpha = 03^h46^m48^s.3\ \delta = +68^\circ05'46.''8$ (J2000)

^bLevine et al. 1993

^cTHH93

^dTH92

Table 3. Measured Temperatures & Intensities

Location ^a	Position	¹² CO(1-0) ^b	¹² CO(2-1) ^b	¹³ CO(1-0) ^b	¹³ CO(2-1) ^b
	(3 ^h 46 ^m , 68 ^o 05')	T_b (K)	T_b (K)	T_b (K)	T_b (K)
	(J2000)	I_{CO} (K kms ⁻¹)	I_{CO} (K kms ⁻¹)	I_{CO} (K kms ⁻¹)	I_{CO} (K kms ⁻¹)
2 μ m peak	(48. ^s 3, 46." ^s 8)	7.4 \pm 1.5	8.6 \pm 2.1	0.9 \pm 0.18	1.23 \pm 0.3
		290 \pm 57	490 \pm 120	41 \pm 8.3	57 \pm 14
NE peak.	(49. ^s 1, 51." ^s 8)	20 \pm 3.9	21 \pm 5.4	2.1 \pm 0.4	2.6 \pm 0.7
		760 \pm 150	1100 \pm 280	61 \pm 12	78 \pm 20
SE peak	(48. ^s 5, 43." ^s 3)	17 \pm 3.4	17 \pm 4.3	1.9 \pm 0.4	2.0 \pm 0.5
		710 \pm 140	790 \pm 200	64 \pm 13	81 \pm 20
SW peak	(47. ^s 5, 41." ^s 9)	15 \pm 3.1	21 \pm 5.2	1.9 \pm 0.4	3.2 \pm 0.8
		630 \pm 130	710 \pm 180	66 \pm 13	86 \pm 22
Off-Arm	(48. ^s 1, 03." ^s 8) ^c	6.5 \pm 1.3	...	0.36 \pm 0.07	...
		52 \pm 10	...	<5	...
Arm	(47. ^s 1, 33." ^s 9)	7.6 \pm 1.5	8.3 \pm 2.1	1.2 \pm 0.24	<0.9
		330 \pm 65	200 \pm 49	31 \pm 6.2	11 \pm 2.7

^aPeaks are based on the ¹²CO(1-0) map.

^b T_b is the Rayleigh-Jeans brightness temperature based on 2."^s7 resolution for ¹²CO(1-0), 4."^s1 resolution for ¹²CO(2-1), 4."^s8 resolution for ¹³CO(1-0) and 4."^s5 resolution for ¹³CO(2-1). Uncertainties are based on the estimated \simeq 20% absolute errors in the (1-0) transitions, and \simeq 25% for the (2-1) transition.

^cbased on $\alpha = 3^h 46^m$ $\delta = 68^o 06'$

Table 4. Measured Line Ratios

Location ^a	$\frac{^{12}\text{CO}(2-1)}{^{12}\text{CO}(1-0)}$ ^{b,c}	$\frac{^{13}\text{CO}(2-1)}{^{13}\text{CO}(1-0)}$ ^{b,c}	$\frac{^{12}\text{CO}(1-0)}{^{13}\text{CO}(1-0)}$ ^{b,c}	$\frac{^{12}\text{CO}(2-1)}{^{13}\text{CO}(2-1)}$ ^{b,c}
	(r ₁₂)	(r ₁₃)	(R ₁₀)	(R ₂₁)
2 μ m peak	1.5 \pm 0.53	1.6 \pm 0.56	7.8 \pm 3.0	10 \pm 3.5
NE ¹² CO(1-0) peak	1.8 \pm 0.63	0.69 \pm 0.24	7.6 \pm 2.7	9.3 \pm 3.3
SE ¹² CO(1-0) peak	1.5 \pm 0.53	0.88 \pm 0.31	7.1 \pm 2.5	7.4 \pm 2.6
SW ¹² CO(1-0) peak	1.4 \pm 0.49	0.93 \pm 0.33	6.6 \pm 2.2	6.0 \pm 2.1
Arm	7.2 \pm 2.5	...
Off-Arm	>18	...

^aSee Table 3 for the positions.

^bRatio based on 4."1 resolution for r₁₂, 4."8 for r₁₃, 4."8 for R₁₀ and 4."5 for R₂₁.

^cSee (§3.3) for uncertainties.

Fig. 1.— a) $^{12}\text{CO}(1-0)$ Integrated intensity map (Levine et al. 1993). Contours are in intervals of $5.0 \text{ Jy Beam}^{-1} \text{ km s}^{-1}$ (or 65.5 K km s^{-1} for the $2.''72 \times 2.''59$ beam). b) $^{12}\text{CO}(2-1)$ Integrated intensity map. Contours are in intervals of $50.0 \text{ Jy Beam}^{-1} \text{ km s}^{-1}$ (or 77.5 K km s^{-1} for the $4.''11 \times 3.''62$ beam). c) $^{13}\text{CO}(1-0)$ Integrated intensity map. Contours are in intervals of $1.50 \text{ Jy Beam}^{-1} \text{ km s}^{-1}$ (or 8.1 K km s^{-1} for the $4.''80 \times 3.''89$ beam). d) $^{13}\text{CO}(2-1)$ Integrated intensity map. Contours are in intervals of $10.0 \text{ Jy Beam}^{-1} \text{ km s}^{-1}$ (or 15.9 K km s^{-1} for the $4.''44 \times 3.''58$ beam). The large circles in b & d) represent the 50% cut of the primary beam. The cross marks the optical and $2\mu\text{m}$ peak (Becklin et al. 1980). The slight misalignment of the coordinate tics result from switching from (B1950) to (J2000) coordinates.

Fig. 2.— Schematic model of the nucleus of IC 342, illustrating the regions discussed in the text. The “off-arm” regions are in dark grey, the “arm” region is the interior white, and the central trough is in light grey. The central starburst HII region is the vertical cross-hatched region, while the eastern ridge is in diagonal cross-hatch. The letters Downes et al. (1992) use to label the five giant molecular clouds found in HCN are displayed. For reference, the features are illustrated on top of the same $^{12}\text{CO}(1-0)$ contours as in Figure 2 (minus the second lowest contour).

Fig. 3.— $^{13}\text{CO}(2-1)$ channel map. LSR velocities are listed on each map. The contours are plotted in intervals of $0.26 \text{ Jy Beam}^{-1}$ (or 0.40 K), corresponding to 2σ . The beam is plotted in the bottom left of the first plane. Negative contours are dashed.

Fig. 4.— a) $^{12}\text{CO}(2-1)/^{12}\text{CO}(1-0)$ (r_{12}) line ratio map. The grey scale range is 0.75 - 2.25, with darker shades corresponding to higher ratios. b) $^{13}\text{CO}(2-1)/^{13}\text{CO}(1-0)$ (r_{13}) line ratio. The grey scale range is 0.25 - 1.75. c) $^{12}\text{CO}(1-0)/^{13}\text{CO}(1-0)$ (R_{10}) line ratio. The grayscale range is 4.0 - 12.0. d) $^{12}\text{CO}(2-1)/^{13}\text{CO}(2-1)$ (R_{21}) line ratio. The grey scale range is 4.0 - 12.0. As a reference, the $^{12}\text{CO}(1-0)$ Integrated intensity map is overlaid on each ratio map.

Contours are in intervals of $11.4 \text{ Jy Beam}^{-1} \text{ km s}^{-1}$ or 150 K km s^{-1} . Ratio are displayed when emission in both maps are greater than 4σ . The slight misalignment of the coordinate tics result from switching from (B1950) to (J2000) coordinates.

Fig. 5.— The HST archive $\text{H}\alpha$ image of the nucleus of IC 342 (Gallagher et al. 1998). The $\text{H}\alpha$ peak flux is $1.2 \times 10^{-16} \text{ ergs s}^{-1} \text{ cm}^{-2}$. For comparison, contours from $^{13}\text{CO}(2-1)$ and 2 cm radio continuum emission are shown. The $^{13}\text{CO}(2-1)$ emission is contoured in thick grey contours, with the same values as in Figure 1d. The 2 cm radio continuum is contoured with thin black contours in multiples of $0.4 \text{ mJy Beam}^{-1} (2\sigma)$. Negative contours are dashed.

Fig. 6.— The results of ^{13}CO LVG modeling of the different regions of the nucleus of IC 342. The contoured regions represent the 1σ confidence solution to both the observed antenna temperature and observed r_{13} . The best fit solution for each region is marked with its corresponding letter designation, A, E & C, for the GMCs, B for the starburst region, and CT for the central trough. The models make use of an abundance ratio of $[^{13}\text{CO}/\text{H}_2] = 2 \times 10^{-6}$. The velocity gradient used is measured directly from the map (FWHM linewidth/FWHM cloud size) and range from $3.4 \text{ km s}^{-1} \text{ pc}^{-2}$ (A, C, E, & CT) to $4.5 \text{ km s}^{-1} \text{ pc}^{-2}$ (B). Therefore, we display two sets of solutions, the thin black line for $3 \text{ km s}^{-1} \text{ pc}^{-2}$ and the thick grey line for $5 \text{ km s}^{-1} \text{ pc}^{-2}$.

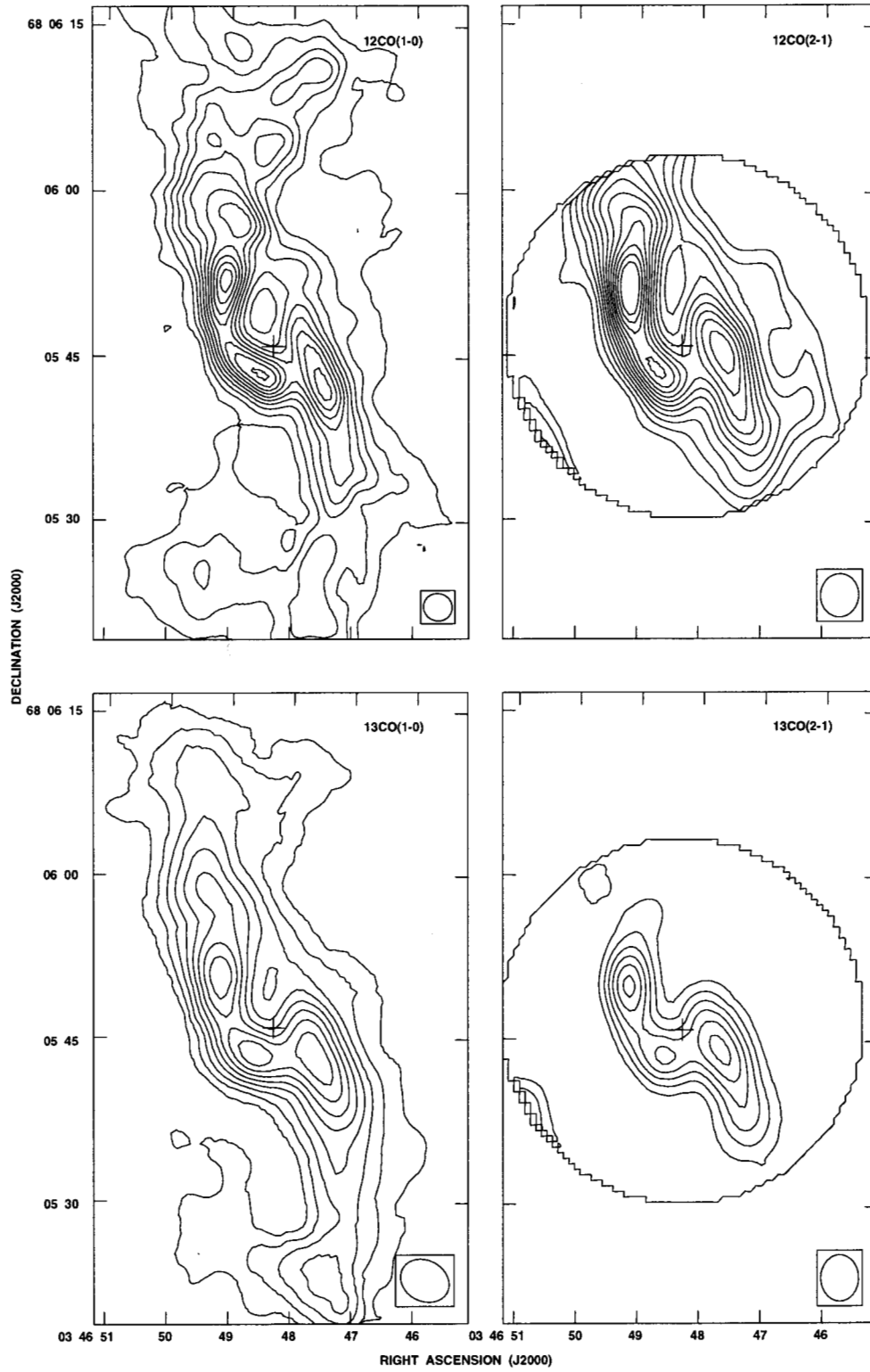


Fig. 1.—

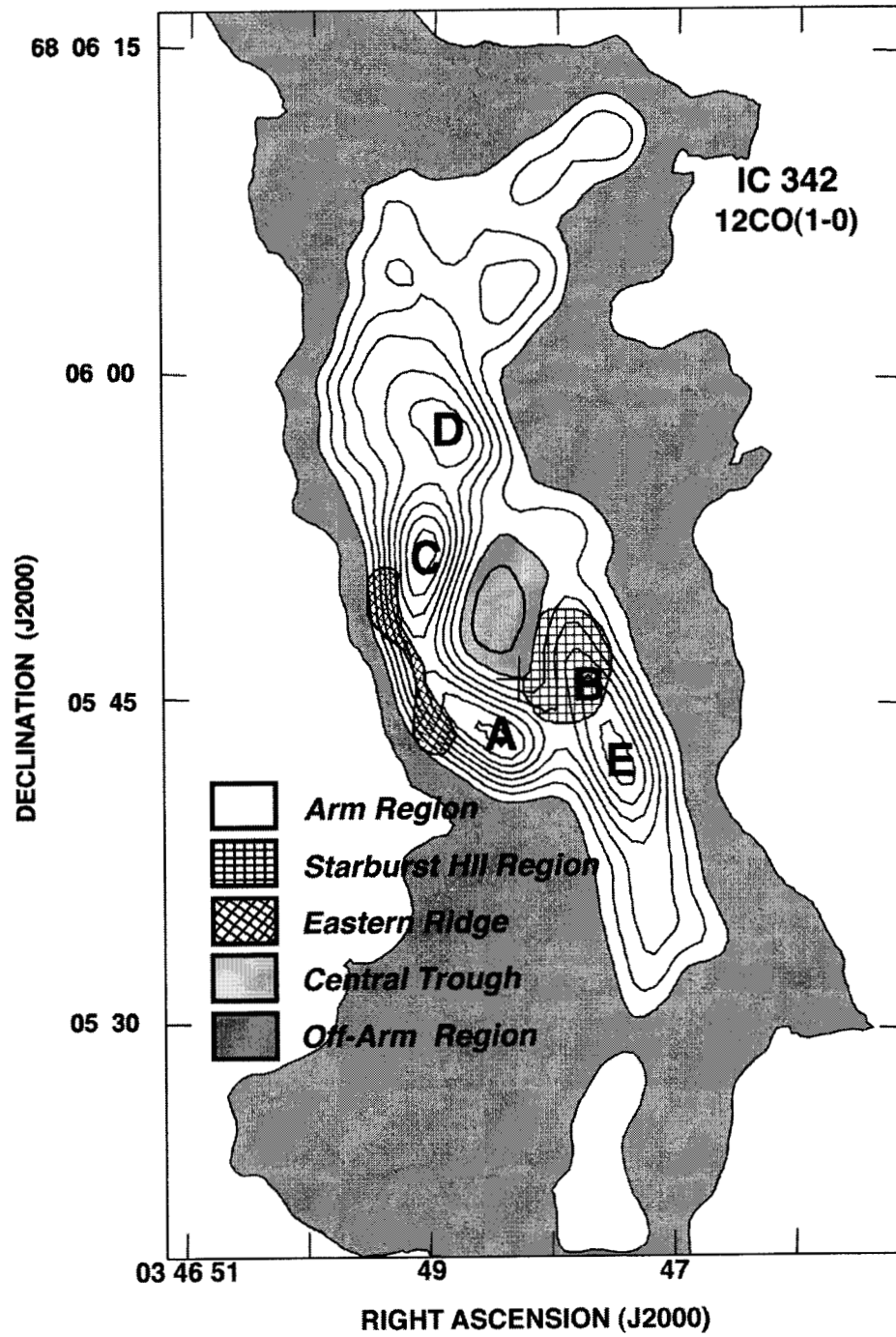


Fig. 2.—

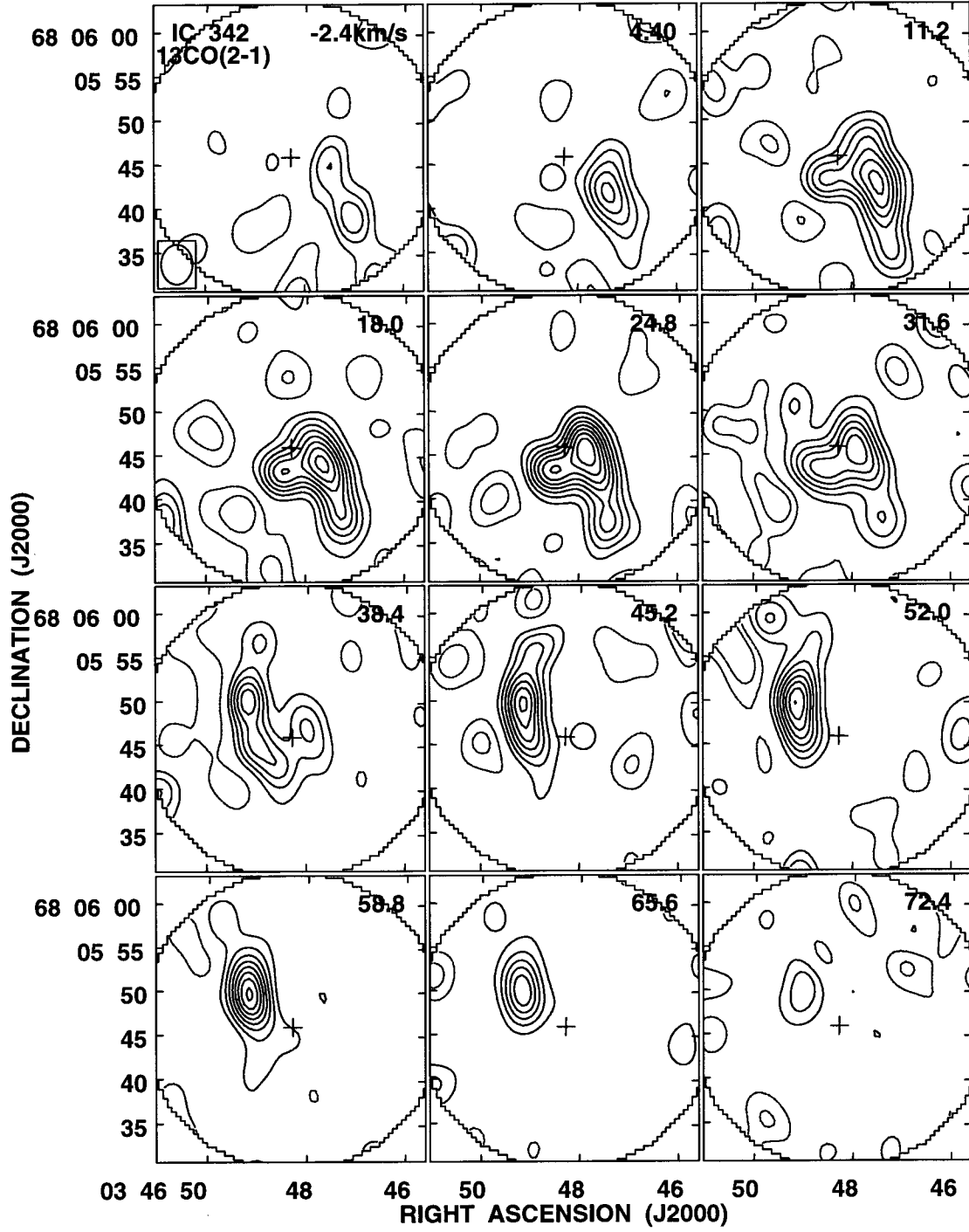


Fig. 3.—

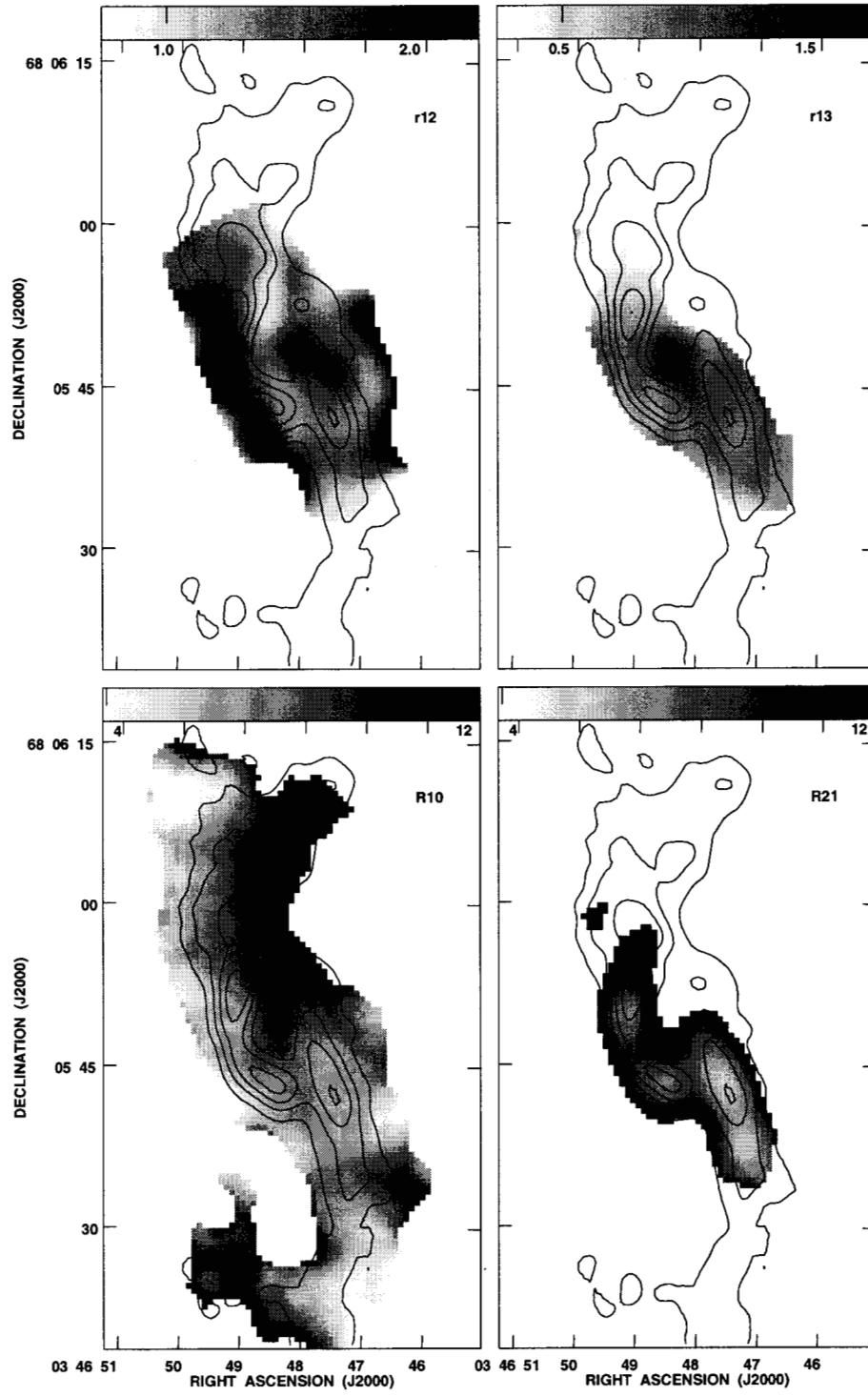


Fig. 4.—

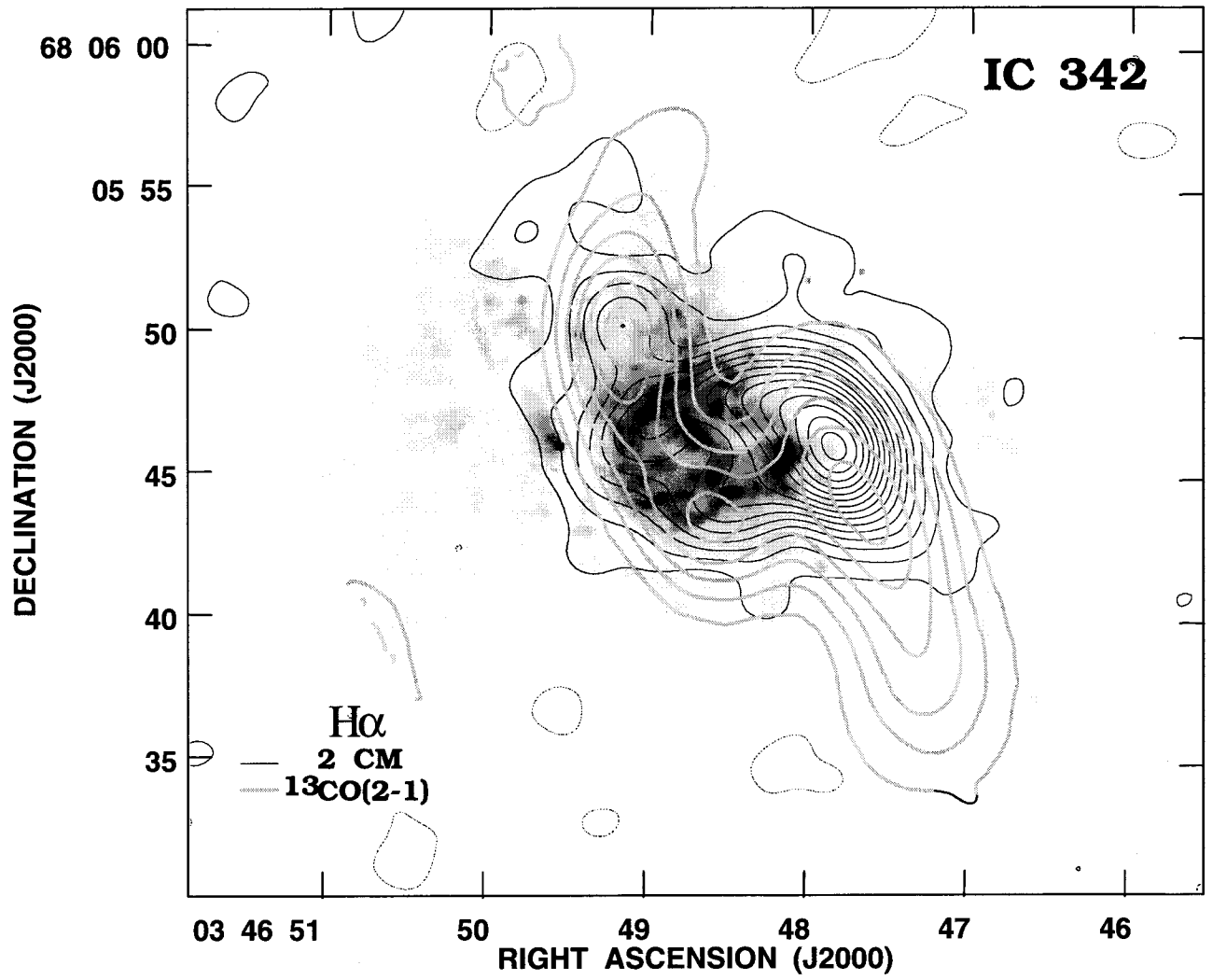


Fig. 5.—

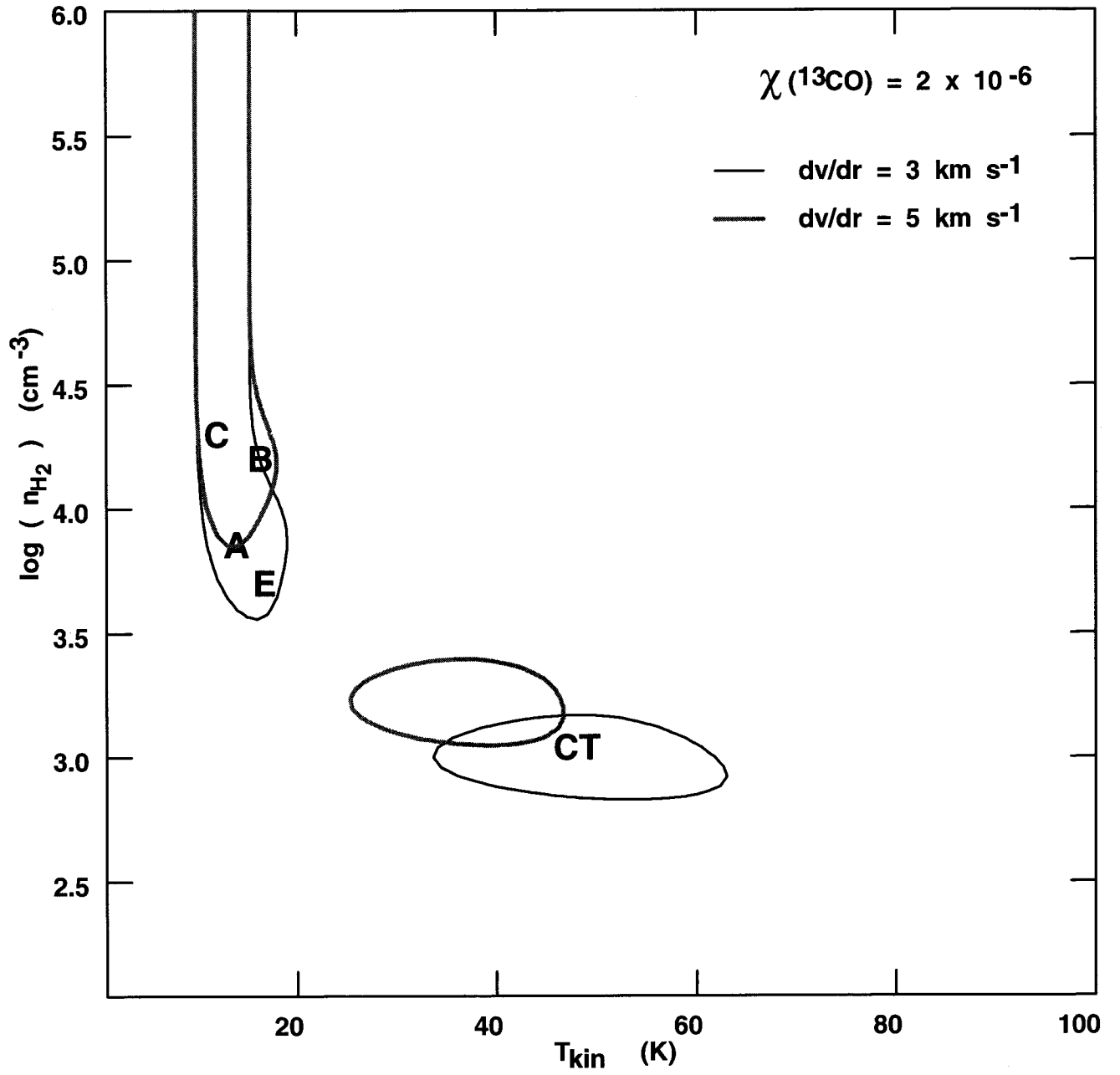


Fig. 6.—